Spatio-temporal non-localities in a solar-like mean-field dynamo

V.V. Pipin

23 February 2023

ABSTRACT

We study how the nonlocal effects of the mean electromotive force affects the mean-field solar type dynamo model. Following suggestion of Rheinhardt & Brandenburg (2012) we approximate the integro-differential equation for the mean electromotive force by the reaction–diffusion type equation. This generalization alleviates the scale separation approximation. Solution of the eigenvalue problem reveals a few curious properties of the dynamo model with the nonlocal mean electromotive force. Besides a decrease of the critical dynamo instability threshold, reported in earlier studies, there is an increase the dynamo periods of the unstable modes. Simultaneously, the nonlocal model shows substantially lower growth rate of the unstable dynamo modes in vicinity above the critical threshold than the model which employ the scale separation approximation. Also, for the nonlocal model, we find a number of the different oscillating and steady dynamo modes can be excited in the close vicinity of threshold of the first unstable dynamo mode. We verify these findings using the nonlinear dynamo model. The model shows the Parker's dynamo wave solutions with the wave propagating from the mid latitude at the bottom of the convection zone toward the solar equator at the surface. In the weakly nonlinear regime, the interference of the dynamo mode of different spatial localization results into the Grand activity cycles of a period about 300 years.

Key words: Sun: magnetic fields; Sun: oscillations; sunspots

Institute of Solar-Terrestrial Physics, Russian Academy of Sciences, Irkutsk, 664033, Russia

1 INTRODUCTION

Since Parker (1955), the standard scenario of the solar magnetic cycle is based on the hydromagnetic dynamo, which includes the cyclic transformation between toroidal and poloidal components of the large-scale magnetic field of the Sun. Steenbeck et al. (1966) put this idea on the theoretical background, proposing the mean-field electrodynamics framework. It was summarized in a number of textbooks, see, e.g, Moffatt (1978); Parker (1979); Krause & Rädler (1980) .

The key theoretical ideas can be formulated as follows. Let us consider the high conductive turbulent media and decompose the magnetic field $\mathbf{B}$ and velocity field $\mathbf{U}$ on to mean and fluctuating parts: $\mathbf{B} = \bar{\mathbf{B}} + \mathbf{b}$, $\mathbf{U} = \bar{\mathbf{U}} + \mathbf{u}$. Here, we use the small letters for the fluctuating part of the fields and capital letters with a bar above for the mean fields. Substitution of these decomposition into induction equation and the averaging over ensemble of the random fields give us the evolution equation for the mean magnetic field,

$$\partial_t \bar{\mathbf{B}} = \nabla \times \left(\bar{\boldsymbol{\mathcal{E}}} + \bar{\mathbf{U}} \times \bar{\mathbf{B}} \right), \tag{1}$$

where the mean electromotive force, $\bar{\boldsymbol{\mathcal{E}}}$,

$$\bar{\boldsymbol{\mathcal{E}}} = \overline{\boldsymbol{u} \times \boldsymbol{b}}. \tag{2}$$

It expresses the effects of the turbulence on the mean magnetic field evolution. To calculate $\bar{\boldsymbol{\mathcal{E}}}$, we have to solve the governing equations for the fluctuating velocity and magnetic field. After using the scale separation approximation this can be done analytically, e.g., with the double scale Fourier transform (Roberts & Soward 1975) and the different assumptions about closure of the correlation's chain (see, Roberts & Soward 1975; Kitchatinov et al. 1994; Kleeorin et al. 1996; Rädler & Rheinhardt 2007). Also the numerical estimation of $\bar{\boldsymbol{\mathcal{E}}}$ is possible with the test-field method (Rheinhardt & Brandenburg 2010; Warnecke et al. 2018). In this case we avoid the closure assumptions completely. The general structure of $\bar{\boldsymbol{\mathcal{E}}}$ can be guessed from the properties of symmetries of transformations of the velocity magnetic field and the assumption about scale separation, as well. Following to Krause & Rädler (1980) we write it as the Taylor expansion about spatial variations of the mean magnetic fields,

$$\overline{\mathcal{E}}_i = \alpha_{ij} \overline{B}_j + \eta_{ijk} \partial_k \overline{B}_j + ..., \tag{3}$$

where α_{ij} is the "pseudo-tensor" which changes the sign under reflection symmetry transformation. The α_{ij} can be further decomposed into sum of symmetric an the antisymmetric parts. The symmetric part of the α_{ij} stands for the turbulent generation α-effect, and the antisymmetric part of the tensor, which can be represented by vector, i.e., $\gamma_i \equiv \varepsilon_{ifj} \alpha_{[fj]}$ (e.g., Krause & Rädler 1980) corresponds to the turbulent pumping. The antisymmetric part of the third rank tensor η_{ijk} represents the turbulent eddy diffusivity.

The spatial and temporal scale separation, which is employed in the Eq(3) can be hardly justified by the solar observations. Indeed, the observations show the continuum spectrum of scales in variations of the photospheric magnetic field variation in space (Vidotto 2016). The scale separation in time variations pronounces greater, having two considerable peaks at the scale of the solar rotation period and the second peak corresponds to the 11-th year solar cycle. Still, it shows the continuum spectrum with inclination of 2/3 in between of these peaks (Frick et al. 2020). Similar results were found from observations of the magnetic activity in the solar type stars having the external convective envelope. Moreover, the very active fast rotating stars can demonstrate the continuum temporal spectrum of the magnetic activity (Stepanov et al. 2020). Breaking of the scale separation assumption can be easily seen in solutions of the mean-field solar dynamo models, as well. Those solutions often show strong spatial variations of the mean magnetic field near boundaries of the dynamo domain(Chatterjee et al. 2011; Brandenburg & Chatterjee 2018; Pipin & Kosovichev 2019).

To account the strong variations of the mean magnetic field in space and time we have to retain the higher order derivatives in expression of $\overline{\boldsymbol{\mathcal{E}}}$. Rädler (1976) and Raedler (1980) suggested that the general conditions expression of $\overline{\boldsymbol{\mathcal{E}}}$ should be written as a convolution between an integral kernel and the mean field, e.g.,

$$\mathcal{E}_i = \hat{G}_{ij} * \overline{B}_j, \tag{4}$$

where the asterisk means a convolution in space and time. Similarly to the Eq(3), we can split it into two pieces and write (Rheinhardt & Brandenburg 2012),

$$\mathcal{E}_i = \hat{\alpha}_{ij} * \overline{B}_j + \hat{\eta}_{ijk} * \partial_k \overline{B}_j \tag{5}$$

The direct numerical simulations (see, Brandenburg & Sokoloff 2002; Rheinhardt & Brandenburg 2012; Bendre & Subramanian 2022; Gressel & Elstner 2020) showed that in the spectral space the kernel $\hat{G}$ is close to a Lorentzian form, i.e., $\hat{G} \sim \left(1 + \mathrm{i}\omega\tau + \ell^2 k^2\right)^{-1}$, here τ corresponds to the turbulent turnover time and ℓ characterizes the length scale on which non-locality becomes important. In this paper, similar to Brandenburg & Chatterjee (2018), we accept the hypothesis, $\hat{G} \sim \left(1 + \mathrm{i}\omega\tau + \ell^2 k^2\right)^{-1}$. The Lorentzian form of the kernel G results into the partial equation for the mean electromotive force in parabolic form,

$$\left(1 + \tau\frac{\partial}{\partial t} + a_{\mathcal{E}}\eta_T\nabla^2\right)\overline{\boldsymbol{\mathcal{E}}} \quad = \quad \overline{\boldsymbol{\mathcal{E}}}^{(0)}, \tag{6}$$

$$\overline{\boldsymbol{\mathcal{E}}}^{(0)} \quad = \quad \alpha_{ij}\overline{B}_j + \eta_{ijk}\partial_k\overline{B}_j \tag{7}$$

where, $a_{\mathcal{E}} \approx 0-1$ is the spatial non-locality parameter (Brandenburg & Chatterjee 2018), the RHS of the Eq(7) corresponds to the local expression of the mean electromotive force obtained either numerically, e.g., by the test-field method or analytically using the SOCA (second order correlation approximation), e.g., Roberts & Soward (1975) and Kitchatinov et al. (1994), or the different forms of the tau approximations (see, Kleeorin et al. 1996; Rädler et al. 2003; Pipin 2008) or the other analytical methods. We have to note that unlike SOCA, the tau approximation is also valid for the cases of the developed turbulence characterized by the high Reynolds numbers. Rädler & Rheinhardt (2007) gave the comprehensive discussion of the analytical approaches for calculation of the mean electromotive force.

Our goal is to study effects of the spatio-temporal nonlocalities in the solar type dynamos and to compare them with the reference dynamo model that utilizes the scale separation approximation. We construct the nonlocal model using the zero order approximation of the mean electromotive force ($\overline{\boldsymbol{\mathcal{E}}}^{(0)}$ from the Eq7) obtained with the minimal tau approximation by Pipin (2008). We used it in the reference dynamo model of Pipin & Kosovichev (2019). Next section discusses the model formulation. After that, we consider the results of the eigen value problem and the nonlinear runs of the nonlocal dynamo model. We resume the main findings in the last section of the paper.

2 DYNAMO MODEL

Similarly, to Brandenburg & Chatterjee (2018) we solve the magnetic field evolution using the mean field dynamo induction equation, the Eq(1) and the evolution equation for the mean electromotive force in form of the Eq(6). The mean-field is decomposed into a sum of the poloidal and toroidal components, as follows:

$$\overline{\mathbf{B}} = \hat{\phi}B + \nabla \times \left(A\hat{\phi}\right),$$

The zero order approximation of the mean electromotive force is calculated using the scale separation assumption an the minimal τ approximation (see, Pipin 2008) It reads,

$$\overline{\mathcal{E}}_i^{(0)} = \left(\alpha_{ij} + \gamma_{ij}\right)\overline{B}_j - \eta_{ijk}\nabla_j\overline{B}_k, \tag{8}$$

here, α_{ij} describes the turbulent generation of the magnetic field by helical motions (the α-effect), γ_{ij} describes the turbulent pumping, and η_{ijk} is the eddy magnetic diffusivity tensor. We take their analytical expression from results of Pipin (2008) (hereafter P08). The α-effect tensor includes effects of the magnetic helicity, i.e.,

$$\alpha_{ij} \quad = \quad C_\alpha\psi_\alpha(\beta)\alpha_{ij}^{(H)} + \alpha_{ij}^{(M)}\psi_\alpha(\beta)\frac{\langle\mathbf{a}\cdot\mathbf{b}\rangle\tau_c}{4\pi\overline{\rho}\ell_c^2}, \tag{9}$$

where the full expressions of the kinetic helicity tensor $\alpha_{ij}^{(H)}$ and the magnetic helicity tensor $\alpha_{ij}^{(M)}$ are given in P08 and also in Pipin (2022) (hereafter P22), $\mathbf{a}$ and $\mathbf{b}$ are the fluctuating vector-potential and magnetic field, respectively. The radial profiles of the $\alpha_{ij}^{(H)}$ and $\alpha_{ij}^{(M)}$ depend on the mean density stratification, profile of the convective RMS velocity u_c and on the Coriolis number $\Omega^* = 2\Omega_0\tau_c$, where Ω_0 is the angular velocity of the star and τ_c is the convective turnover time. In our model we assume that the convective turnover time corresponds to the turbulent relaxation time of the $\overline{\boldsymbol{\mathcal{E}}}$. The magnetic quenching function $\psi_\alpha(\beta)$ depends on the parameter $\beta = \left|\overline{\mathbf{B}}\right| / \sqrt{4\pi\overline{\rho}\mathrm{u}_\mathrm{c}^2}$. Its expression, as well as analytical expressions for $\alpha_{ij}^{(H)}$ and $\alpha_{ij}^{(M)}$ are given in Pipin(2008; 2022).

The magnetic helicity density evolution is governed by the balance equation for the total magnetic helicity, $\langle\chi\rangle^{(\mathrm{tot})} = \langle\mathbf{a}\cdot\mathbf{b}\rangle + \overline{\mathbf{A}}\cdot\overline{\mathbf{B}}$, (see, Hubbard & Brandenburg (2012); Pipin et al. (2013); Brandenburg (2018)):

$$\left(\frac{\partial}{\partial t}+\overline{\mathbf{U}}\cdot\boldsymbol{\nabla}\right)\left\langle \chi\right\rangle ^{(\mathrm{tot})}=-\frac{\left\langle \mathbf{a}\cdot\mathbf{b}\right\rangle }{R_{m}\tau_{c}}+\nabla\cdot\eta_{\chi}\nabla\left\langle \mathbf{a}\cdot\mathbf{b}\right\rangle , \quad (10)$$

where, we use $2\eta\langle\mathbf{b}\cdot\mathbf{j}\rangle=\frac{\langle\mathbf{a}\cdot\mathbf{b}\rangle}{R_{m}\tau_{c}}$ (Kleeorin & Rogachevskii 1999). The second term in the RHS defines the diffusive flux of the small-scale magnetic helicity density, we put $\eta_{\chi}=\frac{1}{10}\eta_{T}$ (Mitra et al. 2010); R_m is the magnetic Reynolds number, we employ $R_m = 10^6$.

The anisotropic diffusion tensor was given Pipin (2008) :

$$\eta_{ijk} = 3\eta_{T}\left\{ \left(2f_{1}^{(a)}-f_{2}^{(d)}\right)\varepsilon_{ijk}+2f_{1}^{(a)}\frac{\Omega_{i}\Omega_{n}}{\Omega^{2}}\varepsilon_{jnk}\right\} \quad (11)$$

where

$$\begin{aligned} f_{1}^{(a)} &= \frac{1}{4\Omega^{*\,2}}\left(\left(\Omega^{*\,2}+3\right)\frac{\arctan\Omega^{*}}{\Omega^{*}}-3\right), \\ f_{2}^{(d)} &= \frac{1}{\Omega^{*\,2}}\left(\frac{\arctan\left(\Omega^{*}\right)}{\Omega^{*}}-1\right) \end{aligned}$$

The antisymmetric tensor γ_{ij} stands for the turbulent pumping, which is usually considered (Krivodubskij 1987; Warnecke et al. 2018) as important ingredient of the solar dynamo process. Following to Pipin (2022), we model it as follows,

$$\gamma_{ij} = \gamma_{ij}^{(\Lambda\rho)}+\frac{\alpha_{\mathrm{MLT}}u_{c}}{\gamma}\mathcal{H}\left(\beta\right)\hat{\mathrm{r}}_{\mathrm{n}}\varepsilon_{\mathrm{inj}}, \quad (12)$$

$$\gamma_{ij}^{(\Lambda\rho)} = 3\nu_{T}f_{1}^{(a)}\left\{ \left(\boldsymbol{\Omega}\cdot\boldsymbol{\Lambda}^{(\rho)}\right)\frac{\Omega_{n}}{\Omega^{2}}\varepsilon_{\mathrm{inj}}-\frac{\Omega_{j}}{\Omega^{2}}\varepsilon_{\mathrm{inm}}\Omega_{\mathrm{n}}\Lambda_{\mathrm{m}}^{(\rho)}\right\} \quad (13)$$

where $\boldsymbol{\Lambda}^{(\rho)}=\boldsymbol{\nabla}\log\overline{\rho}$, $\alpha_{\mathrm{MLT}}=1.9$ is the mixing-length theory parameter, γ is the adiabatic exponent, u_c is the RMS convective velocity. The magnetic quenching function $\mathcal{H}\left(\beta\right)$ are given in the above cited paper (also, see, Ruediger & Brandenburg 1995).

We calculate the turbulent parameters using the mixing-length approximation and the profile of the mean entropy.

$$\mathrm{u_{c}}=\frac{\ell_{\mathrm{c}}}{2}\sqrt{-\frac{\mathrm{g}}{2\mathrm{c_{p}}}\frac{\partial\overline{\mathrm{s}}}{\partial\mathrm{r}}}, \quad (14)$$

where $\ell_c = \alpha_{\mathrm{MLT}}H_p$ is the mixing length, $\alpha_{\mathrm{MLT}} = 1.9$ is the mixing length parameter, and H_p is the pressure height scale. The entropy profile is defined by solving the mean-field heat transport equation (see, e.g., P22) for the rotating convection zone. It deals with deviations of the mean entropy from the reference state due to effect of rotation and the heat energy sink and gain from evolution of the large-scale velocity and magnetic field. To calculate the reference profiles of mean thermodynamic parameters, such as entropy, density, temperature and the convective turnover time, τ_c, we use the MESA model (Paxton et al. 2011, 2013). The Eq. (14) defines the profiles of the eddy heat conductivity, χ_T, eddy viscosity, ν_T, and eddy diffusivity, η_T, as follows,

$$\begin{aligned} \chi_{T} &= \frac{\ell^{2}}{6}\sqrt{-\frac{g}{2c_{p}}\frac{\partial\overline{s}}{\partial r}}, && (15)\\ \nu_{T} &= \mathrm{Pr}_{T}\chi_{T}, && (16)\\ \eta_{T} &= \mathrm{Pm_{T}}\nu_{T}, && (17)\\ \eta_{\mathcal{E}} &= a_{\mathcal{E}}\nu_{T}. && (18) \end{aligned}$$

Here, we parameterize the $\overline{\mathcal{E}}$ diffusivity profile with $a_{\mathcal{E}} = 0.1-1$, in following to Brandenburg & Chatterjee (2018). The angular velocity profile, $\Omega\left(r,\theta\right)$, and the meridional circulation, $\overline{\mathbf{U}}^{(m)}$, are defined by conservation of the angular momentum and azimuthal vorticity $\varpi=\left(\nabla\times\overline{\mathbf{U}}^{(m)}\right)$, (Pipin & Kosovichev 2019; Pipin 2022). In this paper we use the kinematic models excluding effects of the $\overline{\mathbf{B}}$ on the large-scale flow and heat transport. The model shows an agreement of the angular velocity profile with helioseismology results for $\mathrm{Pr}_T = 3/4$. The dynamo models with local $\overline{\boldsymbol{\mathcal{E}}}$ show cycle period of 22 years when $\mathrm{Pm}_T = 10$ and $C_\alpha = 0.042$. The level C_α is slightly above the critical threshold, see the results in the next subsection.

Figure 1 shows the profiles of the large-scale flows, the hydrodynamic α effect and the diffusivity profiles. We note the inverse sign of the α effect tensor components and the rotational quenching of the turbulent diffusivity profile toward the bottom of the convection zone (marked by the dashed line). The profile of $\eta_{\mathcal{E}}$ remains unsaturated and it follows the parameters of the reference convection zone model.

3 RESULTS

3.1 Eigenvalue problem

As the first step we consider the eigen value problem. It helps us to define the critical thresholds of the dynamo instability and the eigen modes profiles. In this case we simplify the model further and neglect the overshoot region below the convection zone. At the bottom of the convection zone, $r_b = 0.728R$, we use the superconductor boundary conditions for the mean electromotive force, $\overline{\mathcal{E}}_{\theta,\phi}=0$, $\partial_r\overline{\mathcal{E}}_r = 0$ and for the poloidal potential, $A = 0$. At the top, $r_t = 0.99R$, we put $\partial_r\left(rA\right)=0$, (radial magnetic field), $B = 0$, $\overline{\mathcal{E}}_r = 0$, and $\partial_r\overline{\mathcal{E}}_\theta = 0$. The numerical integration in radius and latitude is done using the Galerkin method. In the radial direction we decompose A, B and $\overline{\boldsymbol{\mathcal{E}}}$ on the Chebyshev polynomials using the Gauss-Lobatto grid with 50 mesh points and in the latitudinal direction we use the associated Legendre polynomials $P_n^1\left(\theta\right)$ and the Gauss-Legendre grid with 72 points from pole to pole. To satisfy the radial boundary conditions we use the basis recombination method (Boyd 2001) . We put the PYTHON code for solution the eigen value problem on ZENODO.

Figure 2 shows the growth rates and frequencies for the first six eigen modes for the dynamo model with the local expression of the mean electromotive force, i.e., $\overline{\boldsymbol{\mathcal{E}}}\equiv\overline{\boldsymbol{\mathcal{E}}}^{(0)}$. Here, we discuss the odd parity modes, which are antisymmetric about the equator. The property of the obtained dynamo modes is close to results of Pipin & Kosovichev (2019). Yet, the full dynamo period is a bit less than theirs. It is about 14 years. The difference is due to the absence of the overshoot region in the given case. The even modes show very similar diagrams except the first instability threshold for them is a bit higher than $C_\alpha^{\mathrm{cr}} \approx 0.04$ for the odd modes. Typically, for this kind of dynamo models the even modes have a higher instability threshold than the odd modes. Also, we did not find them in the nonlinear runs. Therefore we omit their discussion in below.

Figure 3 shows the instability diagram in the nonlocal dynamo model for two cases $a_{\mathcal{E}} = 0.25$, and $a_{\mathcal{E}} = 0.75$. In these cases the instability threshold is lower than for the case of the

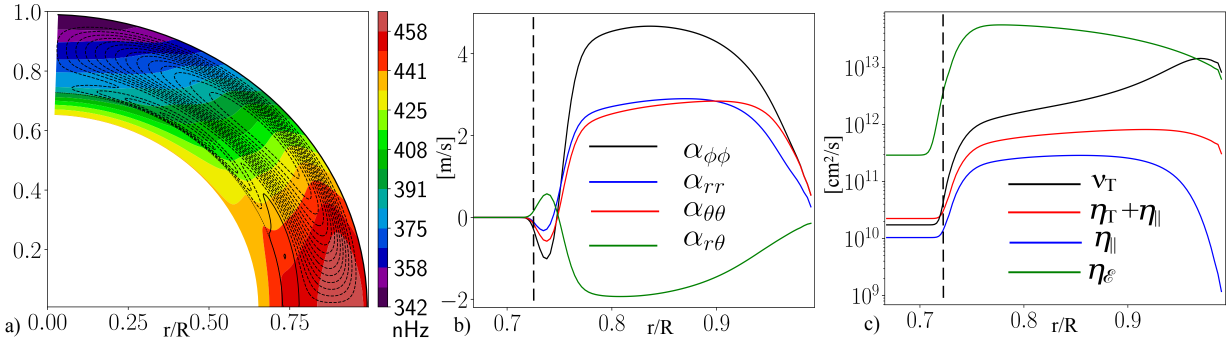

Figure 1. a) The meridional circulation (streamlines) and the angular velocity distributions; the magnitude of circulation velocity is of 13 m/s on the surface at the latitude of 45°; b) the α-effect tensor distributions at the latitude of 45°, the dash line shows the convection zone boundary; b) radial dependencies of the total, $\eta_T + \eta_{||}$, and the rotational induced part, $\eta_{||}$, of the eddy magnetic diffusivity, the eddy viscosity profile, ν_T and the the $\overline{\mathcal{E}}$ diffusivity profile for $a_{\mathcal{E}} = 1$; hereafter we employ NUMPY/SCIPY (Harris et al. 2020; Virtanen et al. 2020) together with MATPLOTLIB (Hunter 2007) for post-processing and visualization.

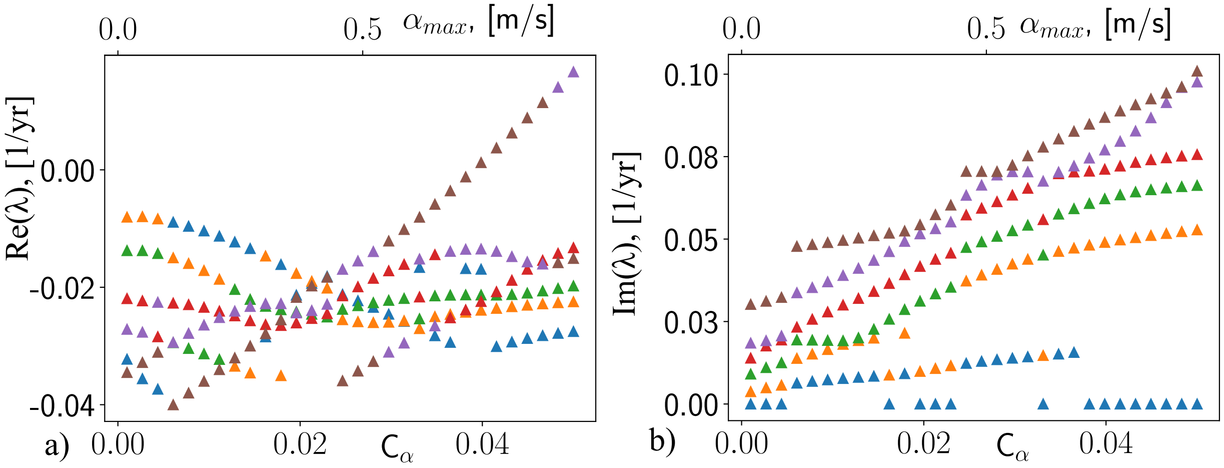

Figure 2. a) Growth rates of the first six eigen odd dynamo modes for the solar type dynamo model with the local mean electromotive force, the x-axis show the maximum magnitude of the $\alpha_{\phi\phi}$ component in the convection zone; colors mark the different eigen modes; b) shows the eigen frequency for each dynamo mode.

model with the local $\overline{\boldsymbol{\mathcal{E}}}$. Brandenburg & Chatterjee (2018) found the same tendency. Also, we see other new features. Firstly, the increase of $a_{\mathcal{E}}$ result into increase of the dynamo period. Secondly, we observe a multiple instability for several dynamo modes when the α effect parameter increases, including the oscillating and steady modes. Thirdly, we find that within the given range of the C_α magnitudes, the growth rates in the nonlocal dynamo are comparable with the local dynamo. The spatial structure of the eigen modes show a difference. It is illustrated in Fig.4. The first unstable dynamo mode for r $a_{\mathcal{E}} = 0.25$ describe the dynamo propagating toward the equator from bottom of the convection zone with the period about 17 years. The second mode, which has the dynamo period of about 64 years, is localized near the bottom of the convection zone. Its propagation can be hardly guessed from a complicated mode structure, see Figs.4 c) and d). We will look at it closely in the next subsection considering the nonlinear solution. The primary feature of this mode is the enhance of the toroidal magnetic field in the polar branch.

3.2 Nonlinear model

The nonlinear dynamo model is based on the model of Pipin & Kosovichev (2019). We consider the models both with include and exclude of the overshoot region. Here, we discuss the kinematic dynamo models, i.e., we neglect effect of the dynamo generated magnetic field on the heat transport and the large-scale flow. In this case the dynamo saturation effects are due to the magnetic helicity conservation, the "algebraic" quenching of α effect and the magnetic buoyancy. We can expect that the last two effects are quenched in depth of the convection zone because of the non-locality (Brandenburg & Chatterjee 2018), which is introduced by diffusivity of the mean electromotive force. The parameters of the nonlinear run are listed in the Table1. To illustrate the nonlinear dynamo solution we choose the case $a_{\mathcal{E}} = 0.5$ ($C_\alpha^{(cr)} = 0.016$) and $a_{\mathcal{E}} = 1$ ($C_\alpha^{(cr)} = 0.013$).

Our basic example is the case N0. The time-latitude diagrams of the toroidal and radial magnetic field evolution are shown in Figure5. We see that the model with the nonlocal $\overline{\boldsymbol{\mathcal{E}}}$ preserves the basic properties of the earlier model of Pipin & Kosovichev (2019). In the upper part of the convection zone

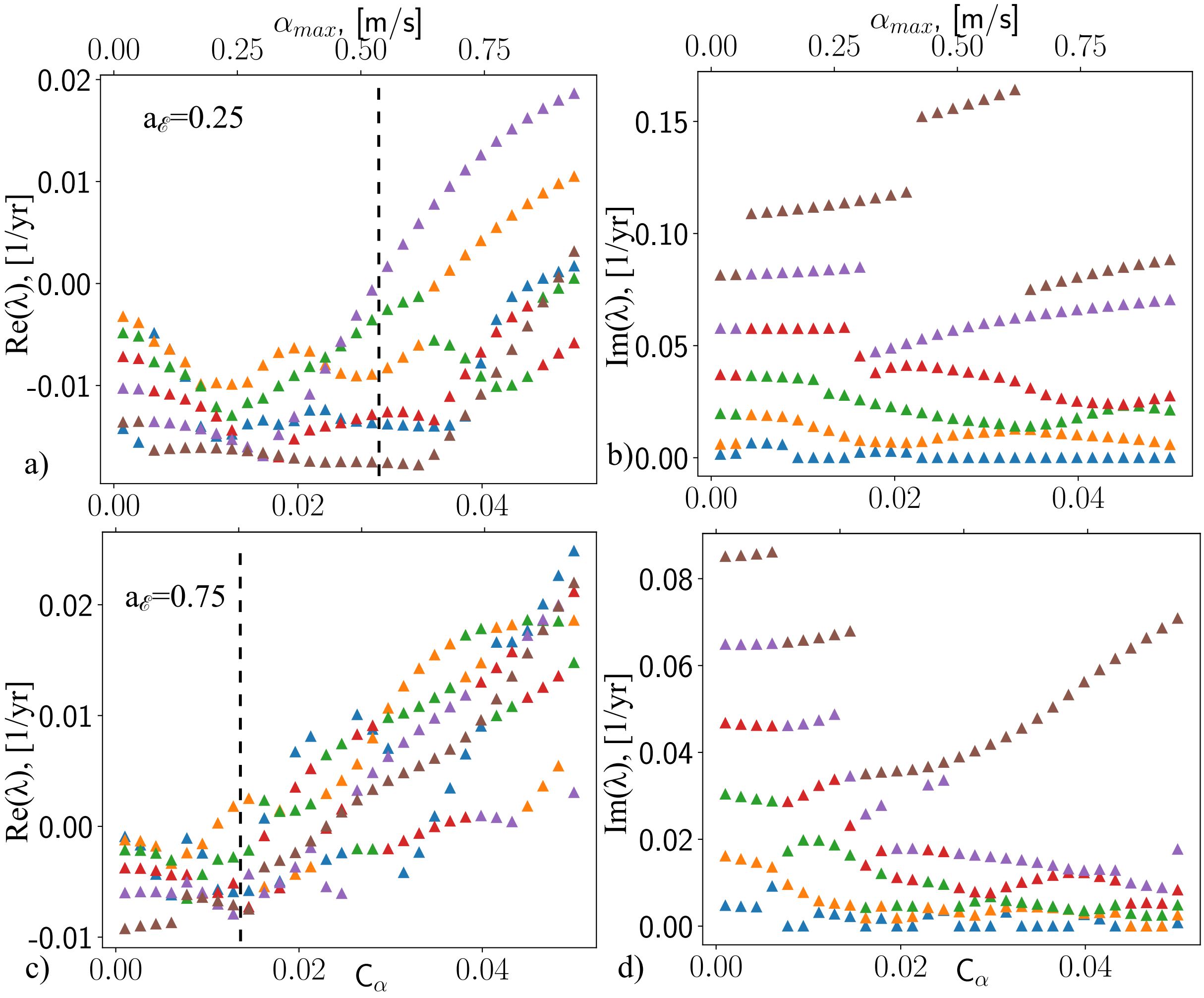

Figure 3. The same as Fig.2 for the nonlocal model with the parameters $a_\mathcal{E} = 0.25$, top row, and $a_\mathcal{E} = 0.75$, bottom row.

Table 1. The parameters of the nonlinear runs. Here, $B_\phi^{(\max)}$ stands for the maximum of the toroidal magnetic field in the convection zone; $B_r^{(>60)}$ is the mean magnitude of the surface radial magnetic field above 60° latitude; F_T is the total unsigned flux of the toroidal magnetic field in the convection zone; P_{cyc} is the half period of the magnetic cycle. We show the parameters of run M25 following results of Pipin (2021), noteworthy,$C_\alpha^{(cr)} = 0.04$ for this case.

	Fig.	$C_\alpha/C_\alpha^{(cr)}$	Overshoot	$a_\mathcal{E}$	$B_\phi^{(\max)}$, [kG]	$B_r^{(>60)}$, [G]	F_T, 10^{24}[Mx]	P_{cyc}, [yr]
N0	5, 6,8	2.2	+	0.5	3.2	6.5	1.	10.9
N1	8	1.1	+	0.5	0.7	0.45	0.11	30.2/25.1/272
N2	8	2.5	+	1	3.5	8.9	1.5	11.8
N3	8	2.2	-	0.5	3.1	3.5	0.9	9
N4	8	2.5	-	1	4.1	5.7	1.2	9.3
N5	7,8	1.1	+	0.75	1.1	0.53	0.13	28/35/326
M25	8	1.1	+	0	2.5	5.6	1.1	10.6

the dynamo wave of the toroidal magnetic field drifts toward the equator. Similar to the above cited paper, this effect results from the joint action of the latitudinal pumping, meridional circulation and the Parker-Yoshimura rule(Yoshimura 1975). Noteworthy, the magnitude of the α effect in run N0 is less than the instability threshold of the reference case model with the local $\overline{\boldsymbol{\mathcal{E}}}$. At the surface the radial magnetic field drifts toward the poles at high latitudes and toward the equator at low latitudes. The polarity sign of these branches corresponds to the leading and following polarity of the sunspot activity. Interesting that both the toroidal and radial magnetic field show the extended 20 yrs branches of activity in overshoot region. This can be important for the origin of the solar torsional oscillations.

Figure 6 illustrates snapshots of the magnetic field and mean electromotive force profiles in run N0 for the half of the magnetic cycle. The magnetic activity shows the dynamo waves propagating from the mid latitude at the bottom of

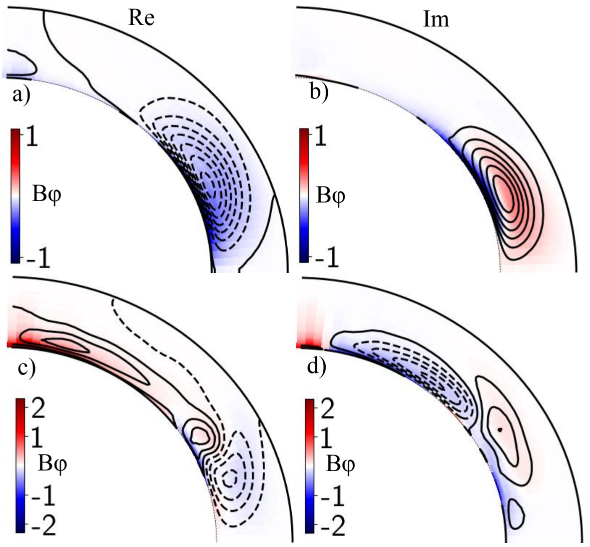

Figure 4. Spatial profiles of the real and imaginary parts of the eigen solution, color shows the toroidal magnetic field and contours show the streamlines of the poloidal field; we normalized the spatial profiles to maximum value. Panels a) and b) show the first unstable mode for the nonlocal model with the parameters $a_{\mathcal{E}} = 0.25$; c) and d) show the same for the second unstable mode.

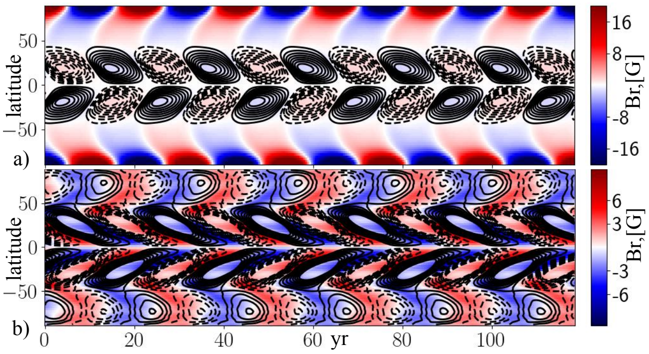

Figure 5. a) The time-latitude diagrams for the run N0, color image shows the surface radial magnetic field and the toroidal magnetic field at r=0.9R, is shown by contours in range ±1.kG; b) the same for the magnetic field in the overshoot layer, r=0.7R.

the convection zone toward equator at the surface. Evolution of the mean electromotive force shows the qualitative similarity to results of the global convection simulations of Racine et al. (2011). Our model shows the two order magnitude less $\overline{\mathcal{E}}_{\phi}$ than the results of the above cited paper. This is because the α threshold for the dynamo instability is order of magnitude less than the mixing length estimation of the convection zone α (cf., Fig.1b and Fig.3). Also, the magnitude of the dynamo generated magnetic field in our model is less than in results of Racine et al. (2011). The difference $\overline{\boldsymbol{\mathcal{E}}}$-$\overline{\boldsymbol{\mathcal{E}}}^{(0)}$ shows the maximum near the bottom of the convection zone, in location of the maximum of the toroidal magnetic field strength. This is because of strong modulation of $\overline{\boldsymbol{\mathcal{E}}}^{(0)}$ by the dynamo generated magnetic field and the increase of $\eta_{\mathcal{E}}$ in the low part of the convection zone.

It is interesting to look at the dynamo solution in vicinity of the instability threshold. The Fig.7 illustrates solution for run N5, where we use a slightly overcritical $C_{\alpha} = 1.1C_{\alpha}^{(cr)}$. The solution show the order of magnitude less strength of the dynamo generated magnetic field than in case N0. In the upper part of the convection zone we find the qualitatively similar pattern of the magnetic field oscillation with the full dynamo period about 60 years and the Grand activity cycle of about 300 year period. The most of the magnetic field flux is concentrated at the interface between the overshoot region and the convection zone. There we see two different patterns of the magnetic field oscillations. At low latitudes the dynamo

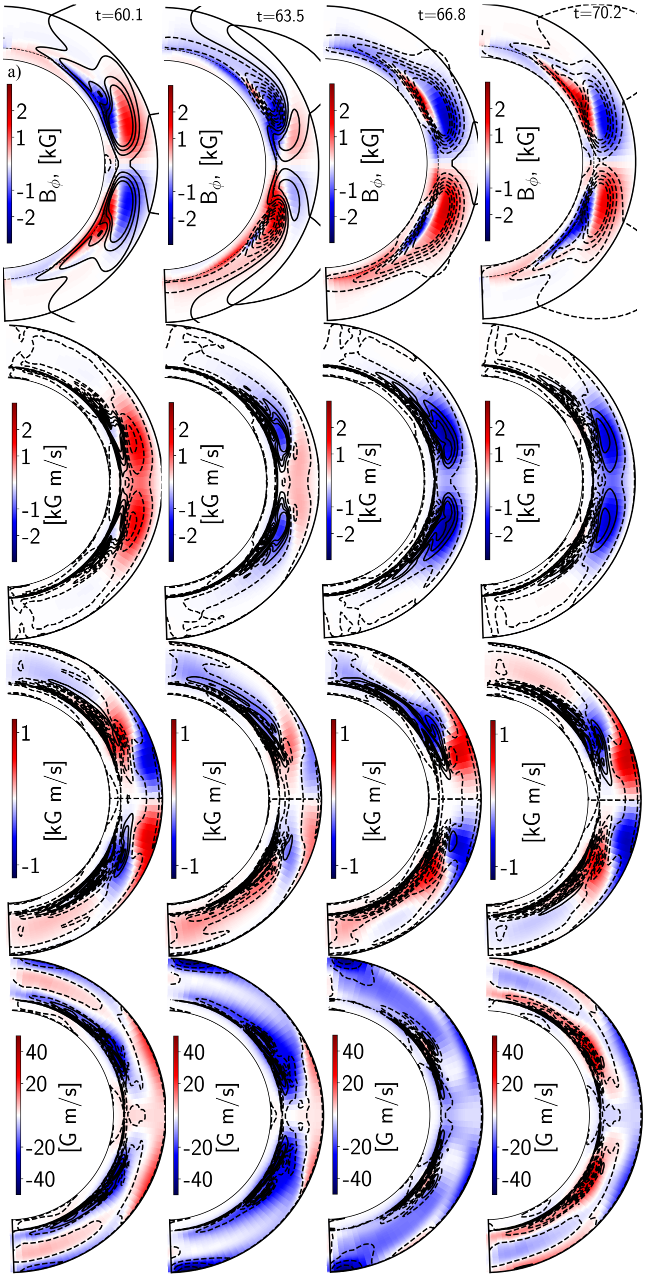

Figure 6. ,a) Snapshots for the magnetic field evolution in run N0 for the half of the activity cycle, contours show streamlines of the poloidal magnetic field; b) color image shows snapshots of $\overline{\mathcal{E}}_r$, contours show the difference $\overline{\mathcal{E}}_r$-$\overline{\mathcal{E}}_r^{(0)}$ for the same range of value as the background color; c) and d) show the same as b) for $\overline{\mathcal{E}}_{\theta}$ and $\overline{\mathcal{E}}_{\phi}$, respectively.

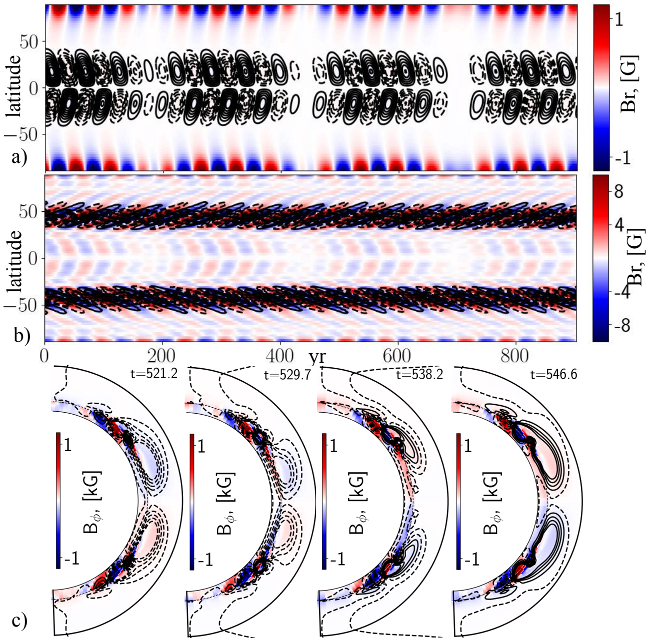

Figure 7. a) The time-latitude diagrams for the run N5, color image shows the surface radial magnetic field and the toroidal magnetic field at r=0.9R, is shown by contours in range ±50G; b) the same for the magnetic field in the overshoot layer, r=0.7R, contours of the toroidal magnetic field are in the range ±1kG; c) snapshots of the magnetic field variations for the half of the magnetic cycle of the equatorward propagating dynamo wave.

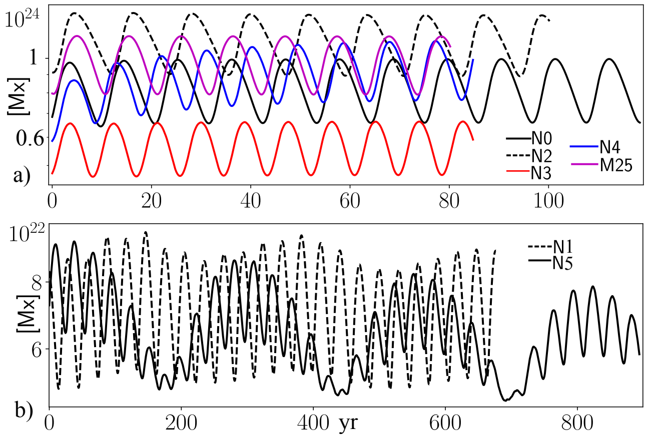

Figure 8. The total unsigned flux of the toroidal magnetic field. a) The runs with the single dynamo wave solution and supercritical $C_\alpha \approx 2.5C_\alpha^{(cr)}$; b) the same for the slightly overcritical $C_\alpha \approx 1.1C_\alpha^{(cr)}$, and $a_{\mathcal{E}} = 0.5$ (N1), $a_{\mathcal{E}} = 0.75$ (N5).

waves propagate toward equator with the period of magnetic activity about 30 years. At the mid latitudes there are waves with a slightly shorter period of around 24 year. The beating of the two dynamo waves of the different localization results to the long-term modulation of the magnetic activity.

The integral parameters of the runs are listed in the Table1. We find that increase of $a_{\mathcal{E}}$ increases the generated magnetic flux. The models which include the overshoot layer show the longer dynamo period than those confined to the convection zone. We find that in nonlinear case an increase of $a_{\mathcal{E}}$from 0.5 to 1 does not result to a substantial increase of the dynamo period. We take the run from Pipin (2021) to compare the solar case dynamo model with our runs. The run M25 (the above cited paper) employs the slightly overcritical $C_\alpha = 1.1C_\alpha^{(cr)}$, where, $C_\alpha^{(cr)} \approx 0.04$, and it has the higher amplitude of the α effect than the N's runs presented here. The run M25 run shows the similar magnitude of the total toroidal flux to the runs N0, N2 and N4. The difference in the dynamo period between the runs is because of lower dynamo instability threshold, $C_\alpha^{(cr)}$, for the nonlocal dynamo model. For the slightly overcritical C_α, the nonlocal dynamo can show the long-term variations of the magnetic activity cycles if the parameter $a_{\mathcal{E}}$ is large enough, see Fig.7a) and Fig.8b). These long-term variations are due to interference of the dynamo modes of different spatial localization, see Fig.7. The run N5 shows two waves of magnetic activity with close periods of 28 and 35 years. These waves start from about 30° latitude and propagate in opposite directions. The mode interaction, because of the non-locality produce the long-term cycle of period 326 years. Interesting that in the run N1 the long-term cycle disappear after a while. In this case, the modes interaction seems to result into nonlinear synchronization of two waves.

We find that the dipole type parity solution dominates in all the runs. In the nonlocal dynamo model the magnetic diffusivity quenching and the meridional circulation result to an increased concentration of the toroidal field to the bottom of the convection zone. The study of Chatterjee et al. (2004) showed that this effects makes the dipole type parity preferable. The question about dependence of this property from the radial profiles of the turbulent parameters should be investigated separately.

4 DISCUSSION

We study effects of the nonlocal mean electromotive force in the solar types dynamo models. Our formulation of the nonlocal $\overline{\boldsymbol{\mathcal{E}}}$ follows the approach suggested by Rheinhardt & Brandenburg (2012) and Brandenburg & Chatterjee (2018). In following the results of the DNS, they suggested that the general integro-differential equation for the mean electromotive force can be replaced by the parabolic equation, see the Eqs(6,7). The temporal non-locality was suggested earlier by Brandenburg et al. (2003) in discussion of the so called minimal τ approximation (Brandenburg & Subramanian 2005). With this approach we formulate the dynamo model that steps over the scale separation approximation. There are both the observational and theoretical requirements for this step. In particular, both the mean-field and flux-transport dynamo models can show a rather strong gradient of the magnetic field near the boundaries of the dynamo domain. We show some examples of this behavior for the distributed mean-field dynamo model in the paper. Also, the solution of the flux transport dynamo model shows several thin magneto shears of the different sign in the close vicinity of the bottom of the convection zone (Dikpati & Charbonneau 1999; Jouve & Brun 2007; Kumar et al. 2019).

The study finds that the mean-field solar type dynamo models preserve their basic properties even with the nonlocal formulation of the mean electromotive force. Similar to Brandenburg & Chatterjee (2018), we find that accounting for non-locality reduces the dynamo instability thresholds. This effect results from the effective eddy diffusivity quenching because of turbulent diffusion of the mean electromotive force. The effect increase the efficiency of the differential rotation and the flux transport by the meridional circulation, as well. The increasing impact of the meridional circulation results in a strong concentration of the toroidal magnetic field toward the bottom of the convection zone. Quenching of the turbulent electromotive force results to some other interesting findings, as well. For example, we see that in the nonlocal model, the growth rate of unstable modes is comparable to local cases for the same magnitude of the α -effect. Reduction of the dynamo instability growth rate is because of saturation of the turbulent generation in the depth of the convection zone. Also, the diffusive quenching of the magnetic buoyancy show the stronger amplitude of the toroidal field in the nonlocal model in compare to the model with local $\overline{\boldsymbol{\mathcal{E}}}$. It is interesting to verify the nonlocal form of $\overline{\boldsymbol{\mathcal{E}}}$ for the α^2 dynamo models.

The decrease of the dynamo instability threshold and the relatively low growth rates in vicinity of the $C_{\alpha}^{(cr)}$ promote generation of the several dynamo modes simultaneously in the weakly nonlinear regime. I this case, the magnetic field evolution concentrates near the bottom of the convection zone and the different dynamo modes show the different dynamo period and different localization. Their interference result to the long-term variation solution for the weakly nonlinear case if the parameter $a_{\mathcal{E}}$ is large enough and C_{α} is close $C_{\alpha}^{(cr)}$. This phenomenon has the same nature as the long-term oscillations because of the parity interaction of the two dynamo modes with close frequency (Ivanova & Ruzmaikin 1976; Brandenburg et al. 1989). Here, we have the dynamo modes of the same parity but the different localization and different directions of the dynamo wave propagation (see, Fig7). The situation is completely different for the supercritical cases when $C_{\alpha}>2C_{\alpha}^{(cr)}$, where the only one dynamo mode survives, while the dynamo instability analysis shows the number of the unstable modes.

Finally, the most important result of the paper is that the solar type dynamo model survives in conditions of the nonlocal mean electromotive force after relaxing the two scales separation approximation. Our deal with the turbulent nonlocality effects follows the hint of the DNS (Rheinhardt & Brandenburg 2012; Gressel & Elstner 2020; Bendre & Subramanian 2022). Despite the suggested mean-field model lose the connection with the fundamental physical laws, it demonstrates a reasonable way to study stellar dynamos beyond the mean-field approximations limits.

Acknowledgments

The author thanks the financial support of the Ministry of Science and Higher Education of the Russian Federation (Subsidy No.075-GZ/C3569/278)

REFERENCES

Bendre A. B., Subramanian K., 2022, MNRAS, 511, 4454

Boyd J., 2001, Chebyshev and Fourier Spectram Methods, second edition edn. Dover, New York

Brandenburg A., 2018, Journal of Plasma Physics, 84, 735840404

Brandenburg A., Chatterjee P., 2018, Astronomische Nachrichten, 339, 118

Brandenburg A., Sokoloff D., 2002, Geophys. Astrophys. Fluid Dyn., 96, 319

Brandenburg A., Subramanian K., 2005, Phys. Rep., 417, 1

Brandenburg A., Krause F., Meinel R., Moss D., Tuominen I., 1989, A&A, 213, 411

Brandenburg A., Blackman E. G., Sarson G. R., 2003, Advances in Space Research, 32, 1835

Chatterjee P., Nandy D., Choudhuri A. R., 2004, A&A, 427, 1019

Chatterjee P., Guerrero G., Brandenburg A., 2011, A&A, 525, A5

Dikpati M., Charbonneau P., 1999, ApJ, 518, 508

Frick P., Sokoloff D., Stepanov R., Pipin V., Usoskin I., 2020, MNRAS, 491, 5572

Gressel O., Elstner D., 2020, MNRAS, 494, 1180

Harris C. R., et al., 2020, Nature, 585, 357

Hubbard A., Brandenburg A., 2012, ApJ, 748, 51

Hunter J. D., 2007, Computing in Science & Engineering, 9, 90

Ivanova T. S., Ruzmaikin A. A., 1976, Soviet Ast., 20, 227

Jouve L., Brun A. S., 2007, A&A, 474, 239

Kitchatinov L. L., Pipin V. V., Ruediger G., 1994, Astronomische Nachrichten, 315, 157

Kleeorin N., Rogachevskii I., 1999, Phys. Rev.E, 59, 6724

Kleeorin N., Mond M., Rogachevskii I., 1996, A&A, 307, 293

Krause F., Rädler K.-H., 1980, Mean-Field Magnetohydrodynamics and Dynamo Theory. Berlin: Akademie-Verlag

Krivodubskij V. N., 1987, Soviet Astronomy Letters, 13, 338

Kumar R., Jouve L., Nandy D., 2019, A&A, 623, A54

Mitra D., Candelaresi S., Chatterjee P., Tavakol R., Brandenburg A., 2010, Astronomische Nachrichten, 331, 130

Moffatt H. K., 1978, Magnetic Field Generation in Electrically Conducting Fluids. Cambridge, England: Cambridge University Press

Parker E., 1955, Astrophys. J., 122, 293

Parker E. N., 1979, Cosmical magnetic fields: Their origin and their activity. Oxford: Clarendon Press

Paxton B., Bildsten L., Dotter A., Herwig F., Lesaffre P., Timmes F., 2011, ApJS, 192, 3

Paxton B., et al., 2013, ApJS, 208, 4

Pipin V. V., 2008, Geophysical and Astrophysical Fluid Dynamics, 102, 21

Pipin V. V., 2021, MNRAS, 502, 2565

Pipin V. V., 2022, MNRAS, 514, 1522

Pipin V. V., Kosovichev A. G., 2019, ApJ, 887, 215

Pipin V. V., Sokoloff D. D., Zhang H., Kuzanyan K. M., 2013, ApJ, 768, 46

Racine É., Charbonneau P., Ghizaru M., Bouchat A., Smolarkiewicz P. K., 2011, ApJ, 735, 46

Rädler K. H., 1976, in Bumba V., Kleczek J., eds, IAU Simposium Vol. 71, Basic Mechanisms of Solar Activity. p. 323

Rädler K.-H., Rheinhardt M., 2007, Geophysical and Astrophysical Fluid Dynamics, 101, 117

Rädler K., Kleeorin N., Rogachevskii I., 2003, Geophysical and Astrophysical Fluid Dynamics, 97, 249

Raedler K.-H., 1980, Astronomische Nachrichten, 301, 101

Rheinhardt M., Brandenburg A., 2010, A&A, 520, A28

Rheinhardt M., Brandenburg A., 2012, Astronomische Nachrichten, 333, 71

Roberts P., Soward A., 1975, Astron. Nachr., 296, 49

Ruediger G., Brandenburg A., 1995, A&A, 296, 557

Steenbeck M., Krause F., Rädler K. H., 1966, Zeitschrift Naturforschung Teil A, 21, 369

Stepanov R., Bondar' N. I., Katsova M. M., Sokoloff D., Frick P., 2020, MNRAS, 495, 3788

Sullivan C. B., Kaszynski A., 2019, Journal of Open Source Software, 4, 1450

Vidotto A. A., 2016, MNRAS, 459, 1533

Virtanen P., et al., 2020, Nature Methods, 17, 261

Warnecke J., Rheinhardt M., Tuomisto S., Käpylä P. J., Käpylä M. J., Brandenburg A., 2018, A&A, 609, A51

Yoshimura H., 1975, ApJ, 201, 740